An instrument to measure the downwelling polarized radiance distribution in the ocean

Purushottum Bhandari, Kenneth J. Voss,* and Luke Logan

Department of Physics, University of Miami, 1320 Campo Sano Ave., Coral Gables, Florida 33146, USA
*voss@physics.miami.edu

Abstract: We have built a new camera system to measure the downwelling polarized radiance distribution in the ocean. This system uses 4 fisheye lenses and coherent fiber bundles behind each image to transmit all 4 fisheye images onto a single camera image. This allows simultaneous images to be collected with 4 unique polarization states, and thus the full Stokes vector of the rapidly changing downwelling light field.

References and links

1. J. S. Tyo, D. L. Goldstein, D. B. Chenault, and J. A. Shaw, "Review of passive imaging polarimetry for remote sensing applications," Appl. Opt. **45**(22), 5453–5469 (2006).
2. R. C. Smith, R. W. Austin, and J. E. Tyler, "An oceanographic radiance distribution camera system," Appl. Opt. **9**(9), 2015–2022 (1970).
3. K. J. Voss and A. L. Chapin, "Upwelling radiance distribution camera system, NURADS," Opt. Express **13**(11), 4250–4262 (2005).
4. H. Du and K. J. Voss, "Effects of point-spread function on calibration and radiometric accuracy of CCD camera," Appl. Opt. **43**(3), 665–670 (2004).
5. J. A. North and M. J. Duggin, "Stokes vector imaging of the polarized sky-dome," Appl. Opt. **36**(3), 723–730 (1997).
6. G. Horváth, A. Barta, J. Gál, B. Suhai, and O. Haiman, "Ground-based full-sky imaging polarimetry of rapidly changing skies and its use for polarimetric cloud detection," Appl. Opt. **41**(3), 543–559 (2002).
7. K. J. Voss and N. Souaidia, "POLRADS: polarization radiance distribution measurement system," Opt. Express **18**(19), 19672–19680 (2010).
8. Y. Liu and K. J. Voss, "Polarized radiance distribution measurement of skylight. II. Experiment and data," Appl. Opt. **36**(33), 8753–8764 (1997).
9. V. Gruev, R. Perkins, and T. York, "CCD polarization imaging sensor with aluminum nanowire optical filters," Opt. Express **18**(18), 19087–19094 (2010).
10. J. S. Tyo, "Design of optimal polarimeters: maximization of signal-to-noise ratio and minimization of systematic error," Appl. Opt. **41**(4), 619–630 (2002).
11. K. J. Voss and G. Zibordi, ""Radiometric and geometric calibration of a visible spectral electro-optic "Fisheye" camera radiance distribution system," J. Atmos. Ocean. Technol. **6**(4), 652–662 (1989).
12. K. J. Voss and Y. Liu, "Polarized radiance distribution measurements of skylight. I. System description and characterization," Appl. Opt. **36**(24), 6083–6094 (1997).
13. H. Dennis, Goldstein, *Polarized Light* (Marcel Dekker, 2003).
14. P. Bhandari, *The Design of a polarimeter and its use for the study of the variation of downwelling polarized radiance distribution with depth in the ocean*, Ph.D. Thesis, University of Miami (2011)
15. A. Ivanoff and T. H. Waterman, "Elliptical polarization in submarine illumination," J. Mar. Res. **16**, 255–282 (1958).

1. Introduction

The spectral polarized radiance distribution provides the most complete set of information on the light field at a given point. To measure the complete polarization of the light field a minimum of 4 different polarization states must be measured for every direction [1]. A convenient method to measure multiple directions of the light field is with fisheye lenses [2,3]. This has the advantage of making measurements of the whole hemispherical field in one image, however there are problems due to internal lens scattering that must be considered [4]. There are at least 3 methods of obtaining the necessary polarization data with the fisheye lens. Systems have been reported that have used multiple camera systems to obtain simultaneous images for both the atmosphere and the ocean [5–7]. In these systems each camera must have

it's own spectral filters, and there can be small variations due to the individual systems characteristics. They must be carefully bore sighted to allow the data to be co-registered. The systems must be carefully synchronized, with accurate shutter timing between the different camera systems.

The second method is to use a series of measurements, inserting different polarizers into the optical train for each measurement [8]. This has been done primarily in the atmosphere, where in clear sky conditions, the sky can be stable enough to assume that the 4 images can be combined separately. In our application this is not a reasonable assumption as the downwelling light field in the ocean is quite dynamic due to the variations of the air-sea interface, and hence the refraction at this interface.

Recently cameras have been reported that would allow at least the linear portions of the radiance distribution to be obtained with a single image, by placing polarizers on the individual pixels of the camera array [9]. This last method is very promising, but no arrays are commercially available at this time.

We chose to design a system around the first method. However, to avoid problems with separate camera systems, we devised a system that collected images from four fisheye cameras, with their own polarizers, onto a single camera image. In this way all four fisheye images use the same spectral filter, the same shutter, and synchronicity between the images is absolutely maintained. However, other difficulties are introduced, which will be described below. We will be describing this system and some of the unique calibration steps beyond those described in earlier papers.

2. General instrument description

The new aspect of the downwelling polarized radiance distribution measurement system (DPOL) is the use of 4 coherent fiber bundles to collect the images from the 4 fisheye lenses, combine the four fiber bundles into one image, and then image this combined bundle onto a camera. In this manner one camera image contains the data for 4 polarization states for a hemisphere of the radiance distribution. A more detailed description follows.

The first optical element of the DPOL system is a non-coated hemispherical custom glass window (inner and outer diameter of 7.62 and 8.26 cm, Outland Technology). The center of the radius of these windows is at the 1st principal plane of the optics. In this manner the light entering the system is perpendicular to the glass window, and thus the system acts the same in air and water.

We use a Coastal Optics c-mount fisheye lens (fl = 2.16 mm, F# = f/3.3-f/16 f-number, 185 deg field of view). We found that this lens, when placed between crossed polarizers, maintained an extinction ratio greater than 100:1 for all angles of incidence. Behind each of the first three fisheye lenses is a linear polarizer (Melles Griot, 03 FPG 019) and behind the fourth lens is a circular analyzer. The three linear polarizers are oriented at approximately 0°, 60° and 120° relative to an arbitrary reference axis [10]. The circular analyzer is a combination of a broadband mica quarter wave plate (Melles Griot, 02 WRM001) and a linear polarizer (Melles Griot, 03 FPG 019).

The fisheye lens forms an 8 mm diameter image on the end of a fiber optic taper that reduces the image size to match the 4 mm x 4 mm coherent fiber optic bundle (Schott North America, Inc.). The other ends of the four bundles are brought together to form a 2 x 2 array of individual fisheye images which is imaged through a spectral filter wheel (Optec IFW), using a lens relay system, onto a CCD camera. Thus all four polarization images are obtained with the same spectral filter and the lens relay reduces the incident angles of the light bundle through the spectral filters. The filter wheel has positions for eight 25.4 mm diameter filters. In 7 positions we insert interference filters to select the spectral bands of interest, while the last position is occulted and is used to obtain a dark reading from the camera.

The camera used in this system is an Apogee, Alta E2000 with a monochrome Kodak KAI-2020M CCD interline transfer array (1600 x 1200, with 7.4 x 7.4 micron pixels elements). This system has both an electronic shutter to allow very fast exposure times and has anti-blooming features to help capture the large dynamic range of the downwelling

radiance distribution. By having all four images on the same camera image errors due to the operation of different cameras, small variations in shutter operation, and offsets between camera electronics are eliminated. Figure 1 is a sample image with this system.
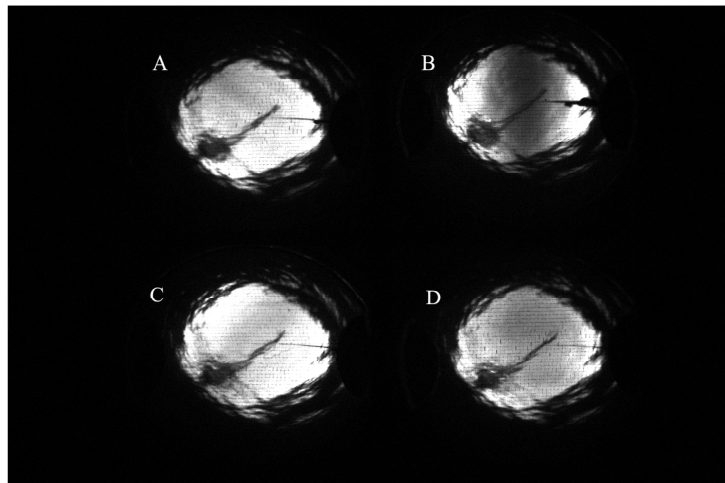

Fig. 1. Sample image from Polarization camera system. There are 4 separate fisheye images shown in this one camera image, the result of our quadfricated fiber bundle. Each small fisheye image carries different polarization information. Three of the images have linear polarizers in line with the image optical path, the remaining image contains a circular polarization analyzer. By combining these images, the 4 Stokes vectors can be determined. Data was at 520 nm, the solar zenith angle was 90°. Data was collected in very clear water off of the Hawaiian Islands from the R/P Flip on September 7, 2009. Measurement depth is 1 m. The area which appears illuminated in this figure is the portion of the in-water radiance distribution with zenith angles from 0 – 48°. The rest of the image is darker because no above-water radiance is refracted into this outer area. Each image has a slightly different illumination pattern because of the interplay between the sky polarization and polarizer for that specific lens. The polarizer arrangements are (angles are with respect to the horizontal axis): (A) Linear polarizer at 60°, (B) linear polarizer at 0°, (C) linear polarizer at 120°, and (D) circular polarization analyzer.

The camera system also has a gyro enhanced orientation sensor (3DM-GX1, Micro Strain), a pressure transducer (Model TJE, Honeywell) to find the instrument depth that gives an analogue output signal (0-5 VDC), directly proportional to the pressure, and other communication electronics. The system communicates to a laptop controller on the surface through an Ethernet link via either fiber or copper, depending on the distances required. The input power required is 28VDC. Figure 2 shows a picture of the instrument after the assembly.

3. Calibration

Most of the calibration steps follow procedures listed in earlier papers for fisheye and polarized fisheye systems [7,11,12]. These calibration/characterization steps include: Linearity, Spectral, Flat-field, Angular or Geometric Calibration (Water and Air), Rolloff Calibration, Polarization Calibration (Linear and Circular), Absolute or Radiometric Calibration, Immersion Calibration, Orientation Sensor Calibration, and Pressure Sensor Calibration. The two calibration steps we will describe in more detail are the flat-field calibration, which is very important in our system because of the irregularities of the transmission in the coherent fiber bundles, and the circular polarization calibration.

Fig. 2. Picture of the top of the polarization camera system. One can see the 4 fisheye lenses all aligned in a row. On the left are connectors to allow the system to be used, either over a dedicated cable (the big connector) or through the ROV system.

3.1 Flat field calibration

Because of non-uniformities in the optical fiber bundle, a uniform source does not produce a uniform image. This comes from a combination of absorbing layers in the bundle and non-uniformities of the individual fiber transmission. In addition there is a variation in transmission at the fiber taper to fiber bundle connection. It is very important to correctly account for these variations, as combinations of pixels, from the separate lenses, are required to obtain the Stokes vector. To do this calibration we expose the ends of the individual fiber bundles (without the lens and polarizer) to the exit port of a 1 m integrating sphere. Light then travels through the fiber bundle and tapers, through the lens relay system and spectral filter, and on to the camera. We then collect 20 to 30 images for each spectral filter that are averaged together to form the flat-field image used in the calibration process and in data reduction. Figure 3 is an example image from this calibration and Fig. 4 shows the effect of the flat-field correction on a horizontal line of data.

To determine the effectiveness of this process another set of data was taken looking into the integrating sphere. The flat-field correction was applied to this image and a 20 x 20 pixel area in the center of the image of the integrating sphere exit port was extracted. The average and standard deviation was calculated for this area. The residual uncertainty, after the flat-field correction, was 5.3%.

3.2. Polarization Calibration

To get polarization information from the images, we must understand how to combine the 4 images to obtain the polarization Stokes vector. Various papers have been published on how to accomplish this (for example [10]). As with most calibration steps, the basic premise is to introduce light with known characteristics (in this case polarization), and measure the instrument's response.
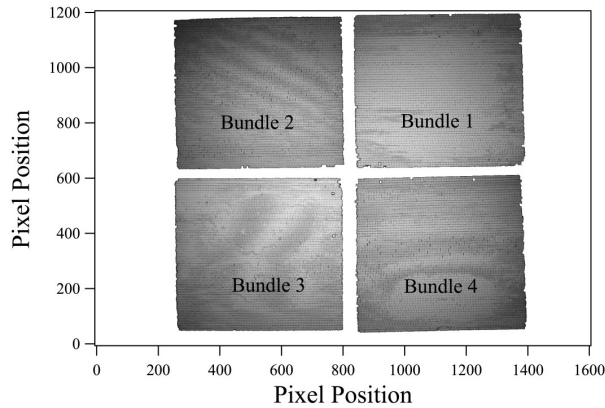
Fig. 3. The image resulting from illuminating the ends of the fibers with an integrating sphere.
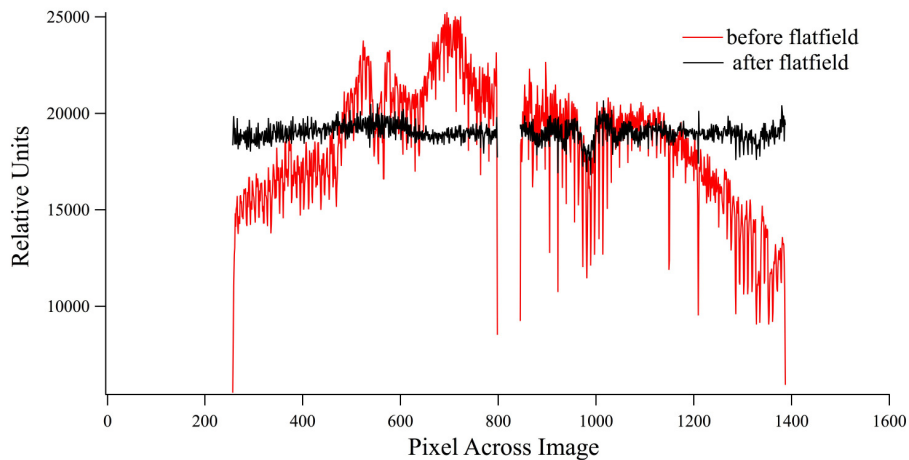

Fig. 4. Example line across a sample image showing the effect of using the flat-field correction.

In our case we illuminate each lens with light with a known polarization state and record the cameras instrument counts. We then performed a multi-variable linear regression with the independent variables being the instruments counts for the 4 sub images, and the dependent variable being *I*, *Q*, *U* or *V* of the incident light. In this way we directly determine the 4 x 4 transformation matrix. This transformation matrix can then be directly used to transform the input intensity information from each lens into normalized Stokes vectors, and then, with an absolute calibration, into S.I. based Stokes vectors.

For this calibration we used a Left-Hand-Circular-Polarizer (LHCP, Alight PFC), which is a combination of a linear polarizer and a quarter wave plate. If the linear polarizer side is towards the DPOL, the LHCP acts as a linear polarizer, reversed it is a circular /elliptical polarizer. In order to know the Stokes vector incident on the camera, we had to characterize the LHCP in terms of its transmission axis (when used as a linear polarizer), retardation angle, and the fast axis angle of the quarter wave plate (when used as a circular polarizer) with respect to a common, but arbitrary, reference axis.

The first step was to determine the transmission axis of the polarization sheet in the LHCP relative to this reference axis. To do this we used a source of monochromatic light from a monochromator (Optronics 740A, and 740 - 20A). Light from the monochromator then goes into the LHCP, with the quarter wave plate towards the light source, and then into a horizontal external polarizer. A simple silicon detector is placed inline to measure the relative intensity transmitted through the system. The LHCP was rotated to find the minimum intensity

(transmission axes of the two polarizers are crossed) and the axis of the polarizer in the LHCP, θ_p, is determined.

To determine the fast axis of the quarter wave plate, and the retardance, the experimental set up is as shown in Fig. 5 and is similar to the previous case except that the LHCP is flipped around. In the Fig. 5, $M_{LP}(\theta_p)$ and $M_{Ret}(\theta_f, \phi)$ represent the linear polarizer and quarter wave plate in the LHCP and $M_{LP}(\theta)$ is the external linear polarizer. The LHCP is fixed with the transmission axis of the linear polarizer held horizontally. For each wavelength used in DPOL, the detector counts were recorded as the external linear polarizer rotated 0-180 degrees in 10 degrees steps.
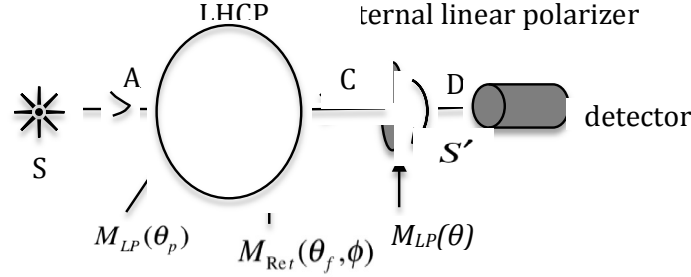

Fig. 5. Experimental set up for the measurement of the fast axis angle and the retardation angle of the LHCP used. S is nearly unpolarized source of monochromatic light.

For this case, the Mueller matrix for a linear polarizer can be represented as follows [13]:

$$
M_{LP} = \begin{bmatrix} 1 & \cos 2\theta & \sin 2\theta & 0 \\ \cos 2\theta & \cos^2 2\theta & \cos 2\theta \sin 2\theta & 0 \\ \sin 2\theta & \cos 2\theta \sin 2\theta & \sin^2 2\theta & 0 \\ 0 & 0 & 0 & 0 \end{bmatrix}. \tag{1}
$$

θ is the angle between the polarizer-preferred transmittance plane and a reference plane.

The Mueller matrix for a retarder having retardation angle ϕ and whose fast axis angle is rotated by an angle θ_ϕ with respect to a reference axis is represented as follows [13]:

$$
M_{ret}(\theta_f, \phi) = \begin{bmatrix} 1 & 0 & 0 & 0 \\ 0 & \cos^2 2\theta_f + \cos\phi \sin^2 2\theta_f & (1-\cos\phi)\sin 2\theta_f \cos 2\theta_f & -\sin\phi \sin 2\theta_f \\ 0 & (1-\cos\phi)\sin 2\theta_f \cos 2\theta_f & \sin^2 2\theta_f + \cos\phi \cos^2 2\theta_f & \sin\phi \cos 2\theta_f \\ 0 & \sin\phi \sin 2\theta_f & -\sin\phi \cos 2\theta_f & \cos\phi \end{bmatrix}. \tag{2}
$$

Then for the Fig. 5, S' at position D can be written as:

$$
S' = M_{LP}(\theta) M_{Ret}(\theta_f, \phi) M_{LP}(\theta_p) S, \tag{3}
$$

where S is the incoming, unpolarized light. Assuming the incoming light is unpolarized, and using Eqs. (1), (2) and (3), the intensity at the detector is given by,

$$
I'(\theta) = 1 + \cos 2\theta \Big[\cos 2\theta_p \left(\cos^2 2\theta_f + \cos\phi \sin^2 2\theta_f \right) + \sin 2\theta_p (1-\cos\phi) \sin 2\theta_f \cos 2\theta_f \Big] \tag{4}
$$
$$
+ \sin 2\theta \Big[\cos 2\theta_p (1-\cos\phi) \sin 2\theta_f \cos 2\theta_f + \sin 2\theta_p \left(\sin^2 2\theta_f + \cos\phi \cos^2 2\theta_f \right) \Big].
$$

From the curve fitting to Eq. (4) we can find the values of θ_f and ϕ for each spectral filter. Table 1 shows these values obtained in the lab and the derived normalized Stokes vector of transmitted light through the polarizer for unpolarized incident light.

Table 1. LHCP Values and Associated Transmitted Stokes Vector for Unpolarized Incident Light

Spectral filters	$\theta_p \pm$ std (degree)	$\theta_f \pm$ std (degree)	$\phi \pm$ std (degree)	Q/I	U/I	V/I
411.1	2.9 ± 0.44	47.6 ± 0.15	104.9 ± 0.15	−0.257	−0.014	0.966
441.6	2.9 ± 0.44	47.4 ± 0.02	103.7 ± 0.06	−0.237	−0.004	0.971
487.7	2.9 ± 0.44	47.4 ± 0.03	103.8 ± 0.07	−0.239	−0.004	0.971
520.6	2.9 ± 0.44	47.5 ± 0.02	88.8 ± 0.03	0.020	0.014	1.000
550.1	2.9 ± 0.44	47.9 ± 0.08	84.7 ± 0.14	0.092	0.008	0.996
589.1	2.9 ± 0.44	48.0 ± 0.09	80.4 ± 0.15	0.166	0.013	0.986
649.2	2.9 ± 0.44	48.4 ± 0.07	73.3 ± 0.10	0.287	0.015	0.958

With θ_p, θ_f, and ϕ, of the LHCP determined we can then use this as a known Stokes vector source for the calibration of DPOL. For this we place the LHCP between an unpolarized uniform source of light (a 1m integrating sphere) and DPOL. Using both sides of the LHCP (circular and linear polarizers), the LHCP is rotated through 180 degrees in 10-degree steps in a clockwise direction as viewed from the source. Because of the physical layout of the instrument, and the port size of the integrating sphere, this was done sequentially for each lens. In each image, an area (5 x 5 pixels) in the center of the illuminated part of the array is extracted as representing the response of the system to that polarization state.

If $I_1(\theta)$, $I_2(\theta)$, $I_3(\theta)$, $I_4(\theta)$ represent the intensities for lens 1, lens 2, lens 3 and lens 4 respectively then we can relate these to the incident Stokes vector in terms of the transformation matrix by the following equation.

$$\begin{bmatrix} 1 \\ Q/I \\ U/I \\ V/I \end{bmatrix} = \begin{bmatrix} T_{11} & T_{12} & T_{13} & T_{14} \\ T_{21} & T_{22} & T_{23} & T_{24} \\ T_{31} & T_{32} & T_{33} & T_{34} \\ T_{41} & T_{42} & T_{43} & T_{44} \end{bmatrix} \begin{bmatrix} I_1(\theta) \\ I_2(\theta) \\ I_3(\theta) \\ I_4(\theta) \end{bmatrix}. \quad [5]$$

By performing the aforementioned multi-variable linear regression for the 38 data points (19 for linear side and 19 for circular side) of Eq. (5), we can determine the 4 x 4 transformation matrix. Note that if we are interested in only the linear polarization calibration then we use only the linear polarization side of the polarizer and the first three lenses of DPOL that have linear polarizer's behind them. In this case we ignore $I_4(\theta)$, V/I, and the fourth row and column in the transformation matrix and obtain a 3 x 3 transformation matrix.

Figure 6 shows the variation in the camera counts as seen by each lens with the rotation of linear (a) and circular (b) polarizer's between the lens and the source.

Figure 7 shows the expected values of the normalized Stokes vectors and the error in generating the Stokes vectors with the transformation matrix, both as a function of polarizer angles of the external polarizer. This error is the difference (predicted – reconstructed) of the normalized Stokes vectors. The average error in these reconstructed vectors is significantly less than 0.02%. The RMS difference is 0.005, 0.009, 0.008 and 0.029 for *I*, *Q/I*, *U/I*, and *V/I* respectively. In this analysis we have not included filter 410 nm because there is insufficient flux from the integrating sphere at this wavelength.
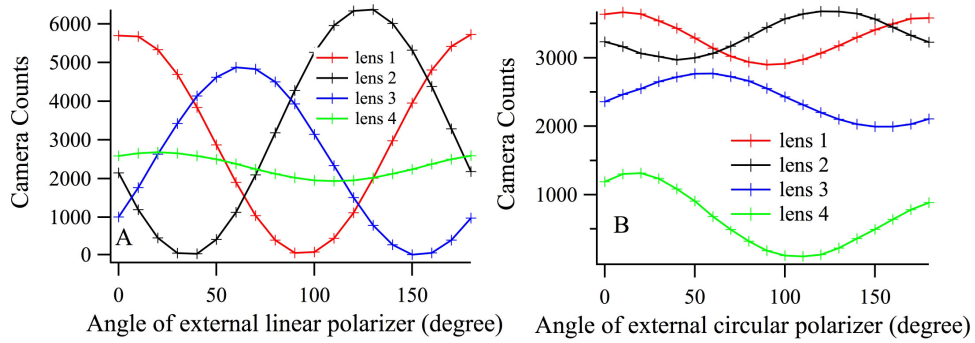
Fig. 6. The camera counts versus the angle of external linear (A) and circular (B) polarizer as seen by the different lenses. Behind lens 1, lens 2, lens 3 are linear polarizers at approximately 0°, 60° and 120° respective to an arbitrary axis and behind the fourth lens is a circular analyzer. In the circular case, lens 4 data has been multiplied by a factor of 10.
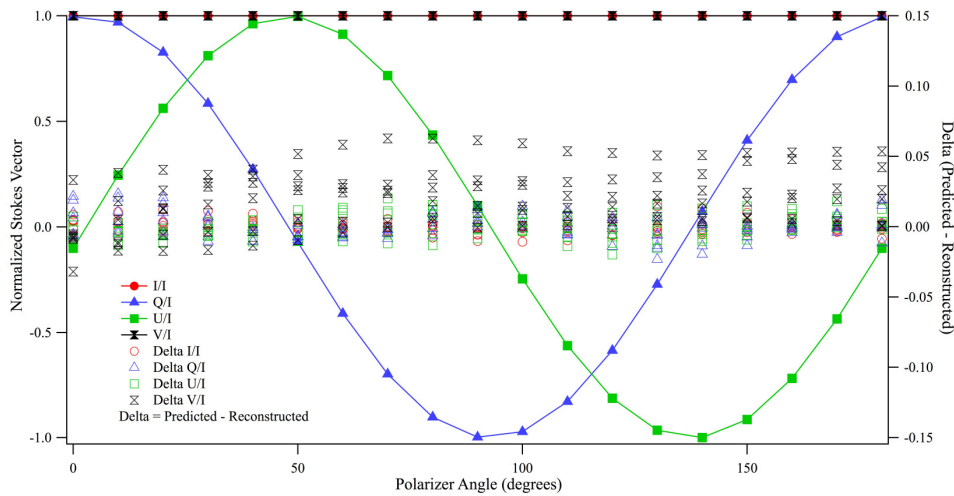

Fig. 7. Normalized Stokes Vectors and difference between predicted and constructed normalized Stokes vectors (Delta).

3.3 Camera sensitivity and dynamic range

During the absolute calibration process we can calculate the range of radiance values which can be measured with the system. The other Stokes parameters (Q, U, and V) are usually reported normalized to this radiance, so the range for these parameters are the same.

To calculate the maximum, we assume a target camera count of 40,000 (a small cushion from the 16 bits available). In testing the camera, we found that the lower limit for shutter speed was 0.007 s, below which the response was non-linear [14]. Using these two assumptions we can calculate the maximum radiance that can be measured for each wavelength, which is shown in Table 2.

To calculate the minimum radiance, we assume a target signal-to-noise ratio of 100. For the downwelling radiance distribution we assume a maximum integration time of 0.03 sec. For the upwelling radiance distribution, where the light field changes more slowly and averaging wave effects is helpful, we assume a maximum integration time of 1 sec. The calculated minimum radiance is also shown in Table 2.

Table 2. Maximum ($L_{max}(\lambda)$) and Minimum ($L_{min}(\lambda)$) Measurable Radiances

Spectral filters	$L_{max}(\lambda)$ μW cm^{-2} nm^{-1} sr^{-1}	Down-welling $L_{min}(\lambda)$ μW cm^{-2} nm^{-1} sr^{-1}	Upwelling $L_{min}(\lambda)$ μW cm^{-2} nm^{-1} sr^{-1}
411.1	1800	4.1	0.12
441.6	490	1.1	0.035
487.7	280	0.64	0.019
520.6	280	0.65	0.020
550.1	390	0.90	0.027
589.1	350	0.82	0.025
649.2	370	0.86	0.026

4. Uncertainty in Stokes vector retrievals

The uncertainty in the retrieval of the Stokes vector and other derived parameters comes from several sources. Since the retrieval process requires using data from each individual camera lens, differences in how each system is characterized can enter into the overall uncertainty or error. Some uncertainties, such as differences in shutter timing between cameras and misalignment of the different cameras is reduced by the design of this system (all lenses mounted on a common machined block and use the same shutter), thus reducing error compared to systems with individual cameras, such as PolRADS [7].

The major source of uncertainty in this system is the residual uncertainty due to the fiber bundle irregularities. To estimate this source of uncertainty we performed the following numerical experiment. We inverted our transformation matrix to determine the intensities that would result for each lens system, with a given Stokes vector input. We then added a random noise factor to each lens intensity that was distributed in a Gaussian fashion, with a width given by the residual uncertainty (5.3%) determined in section 3.1 above. This was done 10000 times, and the resulting mean and standard deviation for the derivation of I, Q, U, and V along with the degree of polarization (DOP) and degree of linear polarization ($DOLP$) was calculated. In all cases the mean I, Q, U and V were retrieved within 0.1%. The standard deviation though varied between the parameters, and averaged 0.03%, 0.05, 0.05, 0.06 for I, Q/I, U/I, and V/I respectively. Because the DOP and $DOLP$ are calculated from the squares of the Q/I, U/I and V/I (the last in the case of DOP), when the DOP or $DOLP$ are large (near 1) the mean value is within 1% of the expected value. The standard deviations for the DOP and $DOLP$ average 0.04 and 0.03 respectively. However, when the input light is unpolarized, because the retrieved values of Q/I, U/I and V/I will bounce around zero, the mean value for the DOP and $DOLP$ was 0.07 and 0.05 respectively, biased slightly high.

The uncertainty in the calculation of the transformation matrix is estimated to be 2% based on the residual errors in the calibration and the uncertainty in deriving each matrix element. There is an additional uncertainty due to the absolute radiance calibration for I that is estimated to be 5% and is due to uncertainties in the lamp irradiance, laboratory setup, and spectralon plaque reflectance. The combination of these uncertainties leads to a measurement uncertainty for I, Q/I, U/I, and V/I of 6%, 0.06, 0.06, and 0.07 respectively. For the DOP and $DOLP$ the uncertainty is 0.05 and 0.04 respectively, but there is an additional bias at low DOP and $DOLP$. The mean values of DOP and $DOLP$ are within 0.01 for expected values >0.20. However for values less than this the positive bias gradually increases and reaches a minimum value for the DOP and $DOLP$ of 0.07 and 0.05 for unpolarized light.

5. Example data

As an example data set, we show derived parameters for the downwelling polarized radiance distribution. This data was collected from the R/P Flip, off of Hawaii, at approximately 4:39 UTC. The measurement depth is 1 m. The water was very clear, the solar zenith angle was 90° as the sun was setting. The wind was 6 m/s, but there were no whitecaps and the surface was not heavily disturbed. This measurement was done at 520 nm.

The following figures are shown in a fisheye format. The center of the images is the zenith direction, zenith angle for the data increases linearly with radius from the center. The two

semicircle cutouts in the data are the clamps that hold on the dome window. Since all four images are required to derive the Stokes vector, the clamps are arranged to block the same portion of each image, this is the main reason the four fisheye lenses are arranged in a line on the instrument. All of these images have been rotated such that the sun is at the top of the image.

Figure 8 shows the downwelling radiance distribution in two formats. Figure 8A is a grey scale representation. Evident in the image is the cable supporting the instrument (line from center and extending upwards) and the supporting boom and R/P Flip extending from the center out towards the edge. The center of the image, out to 48° is the refracted skylight, i.e. Snell's cone, illustrating the "manhole" effect [2]. Outside of this ring the light comes from upwelling light reflecting from the ocean surface, and is therefore much weaker than the refracted skylight. The edge of the Snell's cone is disturbed by surface waves.
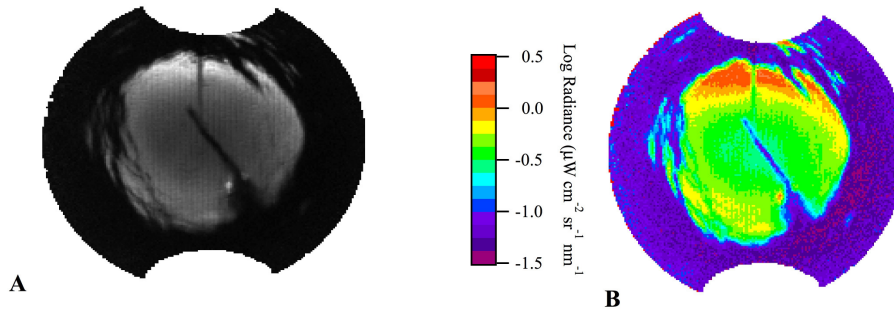

Fig. 8. Radiance (A) and log Radiance (B). In this and the following figures, the zenith angle for the data increases linearly with radius from the center. The two semicircle cutouts in the data are the clamps that hold on the dome window. The sun is towards the top of the image. Data was at 520 nm, the solar zenith angle was 90°. Data was collected in very clear water off of the Hawaiian Islands from the R/P Flip on September 7, 2009. Measurement depth is 1 m.

On the right (Fig. 8B) is the log of the radiance distribution, with false color to be able to determine the radiance values better. At the edge of the Snell's cone the radiance changes by an order of magnitude or more. Even with the direct solar disk not evident in the image, the refracted sky radiance varies by over a factor of 30. If the direct solar disk is in the field of view, at these shallow depths and in clear water, the large radiance (approximately 5 orders of magnitude above the neighboring skylight) causes reflections inside the camera system.

In Fig. 9 we show Q/I, U/I, and V/I for the downwelling lightfield. Q/I, U/I, and V/I (and the plane of polarization, χ) are presented in a frame of reference that is defined relative to the viewing direction. $Q/I = 1$ implies that the plane of linear polarization is in the plane defined by the zenith direction and the viewing direction, while $Q/I = -1$ implies that the polarization plane is 90° to this reference plane. Inside the Snell's cone, the pattern in Q/I and U/I is the same as in the skylight above the surface, and at 1 m the pattern is determined by the polarization of the refracted skylight. Outside of the Snell's cone, the radiance is very low, so while Q/I may look significant, Q is quite low. The edge of the Snell's cone also shows the effects of surface waves. While there are some interesting polarization effects right on the edge, there are also important instrument measurement artifacts to be aware of. The polarization components, Q, U, and V are fundamentally derived from differences between the measurements from each lens, this is evident in the transformation matrix, T, as the 2nd, 3rd, and 4th rows contain negative elements. The radiance, I, is fundamentally an average of the measurements of the first 3, linearly polarized, lenses. At shallow depths, each lens maybe viewing a slightly different portion of the surface for a given direction of view. If one lens is viewing a slightly higher portion of the surface, the result will be a Stokes vector with a

polarization state favoring the polarization of that lens. Since the lenses are separated by 11.2 cm, at 1 m depth this separation may cause a problem, particularly on the edge of the Snell's cone where the radiance is changing rapidly depending on the slope of the surface. Interestingly, this effect should be dampened significantly in the derived radiance, and we still see strong wave surface effects in the radiance.
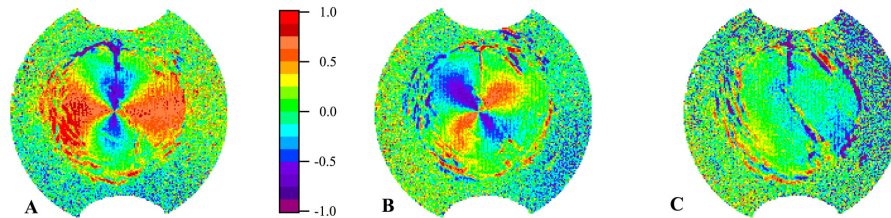

Fig. 9. *Q/I* (A), *U/I* (B), and *V/I* (C) for data shown in Fig. 8.

V/I is quite low, as it was throughout our data sets. There is no significant *V/I* in the sky radiance. There is a small amount of *V/I* thought to be in the subsurface radiance distribution, but only very near the surface, and in very calm days [15].

Figure 10 shows the Degree of Linear Polarization, *DOLP*, and the angle of the plane of polarization, χ. There is a very high *DOLP*, near 80%, which is the result of the refracted skylight, at a scattering angle of 90° in air. The *DOP* was virtually the same as the *DOLP*, since *V/I* is so small. χ variation reflects the varying reference frame in the coordinate system used.
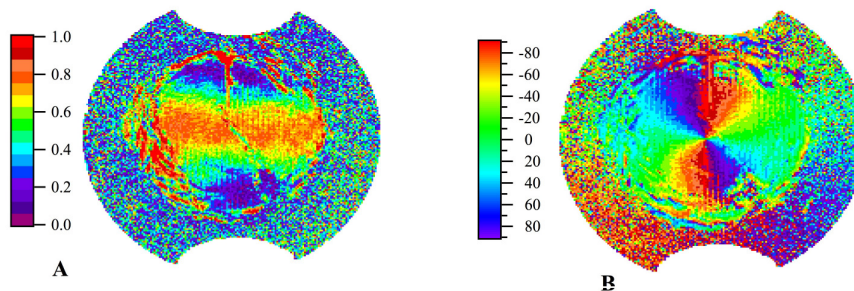

Fig. 10. Degree of linear polarization, *DOLP*, and plane of polarization, χ, for data shown in Fig. 8.

6. Conclusion

We have described a new instrument to measure the upwelling and downwelling spectral polarized radiance distribution in the ocean. This instrument has advantages over the use of separate camera systems since all the images go through the same spectral filter and are imaged on a single CCD array, there can be no variation between the polarization images (which must be mathematically differenced to get the Stokes vector) due to the different cameras. The use of a CCD device as a "still" camera limits how fast images can be obtained, but allows the use of the system over a larger dynamic range of radiances (by adjusting shutter speed). The high intensity resolution, given by the 16-bit resolution, is also required to have sufficient accuracy to perform the transformation into Stokes vectors in images with large

intra-scene dynamic range. The disadvantages of the system revolve, chiefly, around the performance of the fiber optic bundle. The major source of uncertainty results from inhomogeneities in the coherent fiber bundle and fiber taper. Improved performance of the fiber bundle would be required to significantly improve the operation of the system. The fiber bundle limits the spatial resolution of the instrument both because of the inherent fiber size, but also because of the increased averaging required to achieve reasonable uniformity after the flat-field process. Finally, while the CCD array has anti-blooming features, the number of optical surfaces in the system limits the intra-scene dynamic range because of scattering and reflections from the surfaces in the system. The expected accuracy of the radiance, *Q/I*, *U/I*, and *V/I* are 6%, 0.06, 0.06, and 0.07 respectively. The uncertainty of the derived *DOP* and *DOLP* are 0.05 and 0.04 respectively, however there is a positive bias of the *DOP* and *DOLP* for values of the *DOP* and *DOLP* <0.2.

Acknowledgments